Nanoscale

PAPER

View Article Online
View Journal

Cite this: DOI: 10.1039/d0nr00457j

Independent tuning of bright and dark meta-atoms with phase change materials on EIT metasurfaces

Ce Li, [a,b] Wei Zhu, [c] Zhe Liu,[d] Ruhao Pan, [a,b] Sha Hu, [a,b] Shuo Du,[a,b] Junjie Li *[a,b,e] and Changzhi Gu*[a,b,f]

Received 16th January 2020,
Accepted 2nd April 2020

DOI: 10.1039/d0nr00457j

rsc.li/nanoscale

The realization of tunable metasurfaces is of fundamental importance for boosting the electromagnetic field control ability. Especially, it is important to put forward new modulation methods to further understand their underlying modulation mechanism and expand their application range. In this paper, tunable electromagnetically induced transparency (EIT) metasurfaces based on the phase change material $Ge_2Sb_2Te_5$ (GST) are proposed and experimentally demonstrated. Different from previous modulation methods of directly introducing the GST film below the metasurfaces, here a two-step lithography method is introduced to combine independent GST strips with bright and dark meta-atoms in the EIT structures, respectively, achieving the independent modulation of the EIT-like spectra. In addition, by applying temporal coupled-mode theory (TCMT), the EIT-like spectra with different GST crystallization levels were analysed and the corresponding characteristic parameters were determined simultaneously. These fitting results reveal that GST strips can modulate the resonances of the bright and dark meta-atoms independently by shifting the resonant frequency and increasing the decay rate, which in turn result in the different modulation features of the EIT-like spectra. This method improves the degree of freedom of active modulation and provides a new route for tunable slow light devices.

Introduction

Metasurfaces are two-dimensional (2D) or quasi 2D subwavelength-patterned structures that have unique abilities to fully manipulate the light based on specific geometries and arrangement configurations of the constituent elements.[1,2] Compared with the conventional three-dimensional (3D) metamaterials, metasurfaces have shown higher potential for applications because of their compactness and compatibility with on-chip nanophotonic devices.[3,4] In particular, tunable metasurfaces, as a new branch of metasurfaces, are reconfigurable and/or tunable in real time because of their optical characteristics through external control, which leads to a further breakthrough in photonic applications.[5–7] At present, the incorporation of materials with tunable optical or electrical properties, such as graphene,[8–10] semiconductors,[11–13] and phase change materials, is an effective route to modulate original passive metasurfaces.[14–21] It is worth mentioning that the phase change material $Ge_2Sb_2Te_5$ (GST),[22] a ternary chalcogenide alloy, has shown tremendous advantages in realizing metasurface tunability. It has stable amorphous and crystalline states, which can be switched quickly, nonvolatively and reversibly by thermal, electrical or pulse light methods,[23] which makes GST an important candidate for application in data storage and neuro-inspired computing.[24,25] Besides, both the permittivity and electrical conductivity of GST show distinct discrepancies before and after phase transition.[26,27] All these properties promote the rapid development of the fields utilizing GST-based tunable metasurfaces[28] and make it applied in tunable absorbers,[29,30] tunable color display,[19,31] tunable metalens,[23,32] tunable Fano resonance, tunable electromagnetically induced transparency (EIT) resonance,[33–35] *etc.*

EIT is a quantum interference effect that gives rise to a sharp transparent window within a broad absorption spectrum.[36,37] Such a phenomenon was introduced in the field of metasurfaces in 2008 by Zhang *et al.*,[38] and they demon-

[a]*Beijing National Laboratory for Condensed Matter Physics, Institute of Physics, Chinese Academy of Sciences, Beijing 100190, China. E-mail: czgu@iphy.ac.cn, jjli@iphy.ac.cn*
[b]*School of Physical Sciences, CAS Key Laboratory of Vacuum Physics, University of Chinese Academy of Sciences, Beijing 100049, China*
[c]*Key Laboratory of Space Applied Physics and Chemistry, Ministry of Education and Department of Applied Physics, School of Science, Northwestern Polytechnical University, Xi'an 710129, China*
[d]*Niels Bohr Institute, University of Copenhagen, Blegdamsvej 17, DK-2100 Copenhagen, Denmark*
[e]*Songshan Lake Materials Laboratory, Dongguan, Guangdong, 523808, China*
[f]*Collaborative Innovation Center of Quantum Matter, Beijing, China*

strated that coupled bright and dark plasmonic meta-atoms can realize EIT-like optical responses. Besides, the EIT-like resonance can result in a dramatic dispersion, which leads to its potential applications in slow light devices.[39] In addition, the tunability of EIT-like devices[12,35,40–42] is of great significance to further improve their practical application.

In this article, we experimentally demonstrate a new approach to modulate EIT metasurfaces through combining with GST strips. Different from the general method of directly introducing the GST film underneath, here we propose an idea of introducing GST into strip structures and combining them with the bright and dark meta-atoms in the EIT metasurface, respectively. This idea provides a possibility to improve the degree of freedom of active modulation in experiments, because spatially separated GST strip structures can result in the selective modification on the EIT metasurfaces. In addition, the temporal coupled-mode theory (TCMT)[43,44] was utilized to fit the EIT-like transmission spectra and to determine characteristic parameters for different GST crystallization fractions, which proves that GST directly modulates the response of the combined bright or dark meta-atoms through phase transition, resulting in the different modulation effects on EIT-like transparent windows.

Sample preparation and characterization

Fig. 1(a) schematically shows the unit cells of the two kinds of tunable EIT metasurfaces. The total structure is composed of a metal structure layer, a dielectric protective layer, GST strip structures, and a bottom quartz substrate. For the metal structure layer, the upper metal antenna and the lower pair of metal bars in the unit cell represent the bright and dark meta-atoms of the EIT metasurface, respectively. The film with transparent color represents a SiO_2 layer, which can prevent GST from oxidation during the phase transition process. The blue strips embedded in the quartz substrates represent GST strip structures. For convenience, the structure where GST strips are placed underneath the bright meta-atoms is named the bright meta-atom directly modulated metasurface (BMM), and the structure where GST strips are placed underneath the dark meta-atoms is called the dark meta-atom directly modulated metasurface (DMM). The whole structures are excited by a plane wave along the $-z$ direction with the electric field vector $\boldsymbol{E}$ along the x direction. For simplicity, the resonance frequencies of both BMM and DMM are set to be as consistent as possible by adjusting their geometric sizes, respectively.

The designed metasurfaces are applied by nanofabrication, following the process flow shown in Fig. 1(a). To begin with, the PMMA (polymethyl methacrylate) resist was spin-coated on a clean quartz substrate and baked at 180 °C for 1 minute, after which the strip patterns were defined on the resist layer by electron beam lithography (EBL, Jeol 6300FS). Next, 30 nm deep trenches were formed by reactive ion etching (RIE, Oxford PlasmaLab NGP80) with Ar and CHF_3 plasmas. Then, a 30 nm thick GST layer composed of germanium (Ge), antimony (Sb), and telluride (Te) with a ratio of Ge, Sb, Te = 2 : 2 : 5 ($Ge_2Sb_2Te_5$) was deposited *via* magnetron sputtering. Subsequently, the GST strips were formed using an acetone lift-off process. After this, a 20 nm SiO_2 layer was deposited onto the sample surface as the protective layer using a plasma-enhanced chemical vapor deposition (PECVD) system (Oxford PlasmaLab 100). To avoid the phase change of GST caused by regular high temperature, the deposition temperature was controlled at 110 °C. Then the second EBL step was performed to

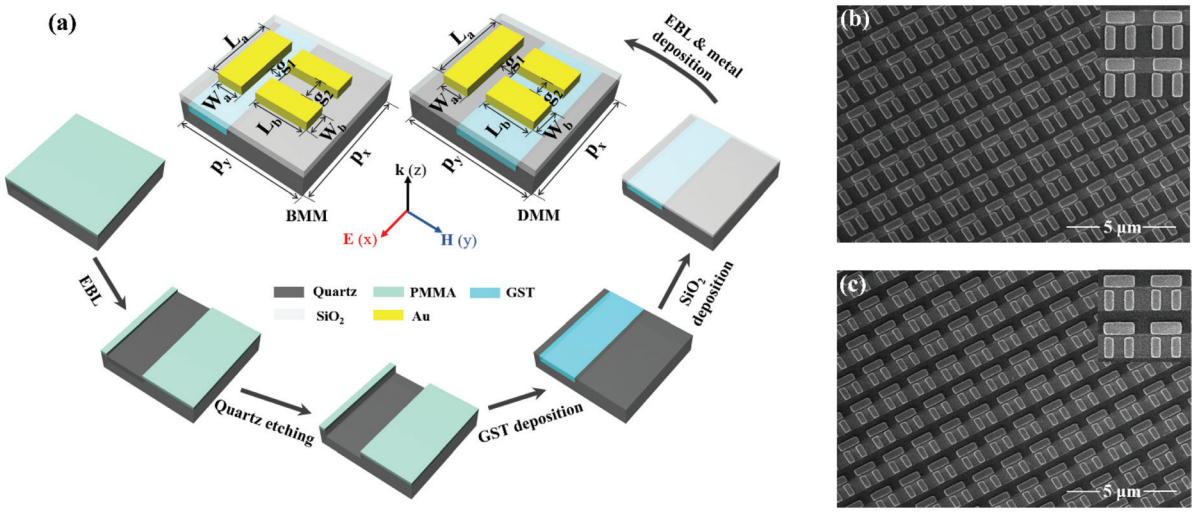

Fig. 1 (a) Schematic of the fabrication process of the tunable EIT metasurface and the magnified schematic of the BMM and DMM unit cell with labeled dimensions. The geometric sizes of the BM structure are L_a = 880 nm, W_a = 360 nm, L_b = 750 nm, W_b = 300 nm, g_1 = 85 nm, and g_2 = 340 nm. The geometric sizes of the DM structure are L_a = 980 nm, W_a = 320 nm, L_b = 660 nm, W_b = 300 nm, g_1 = 110 nm, and g_2 = 320 nm. Besides, both of the structures have the same period $p_x = p_y$ = 1.5 μm. The thickness of GST strips is 30 nm, and the thicknesses of the SiO_2 protective layer and Au structures are 20 nm and 60 nm (not labeled in the schematic diagram), respectively. (b and c) SEM images of BMM and DMM.

pattern the metasurface arrays with the PMMA resist. For BMM, the bright meta-atoms were aligned with the GST strips, while for DMM, the dark meta-atoms were aligned with the GST strips. After this, 3 nm Cr and 60 nm Au films were deposited onto the samples using electron beam evaporation. Followed by the lift-off process, the whole metasurface arrays with GST strips and the SiO_2 protective layer were completed. Both the periods of the two configurations are $p_x = p_y = 1.5$ μm; other geometric parameters are listed in detail in the legend of Fig. 1. The total array size is 100 × 100 μm^2, which is large enough to satisfy the measurement requirements. The scanning electron microscopy (SEM) images of the fabricated BMM and DMM are shown in Fig. 1(b) and (c), respectively.

The GST phase transition process was performed using a rapid thermal annealing (RTA) system at 260 °C in N_2 forming gas for 5 minutes. The phase transition temperature is higher than that mentioned in the previous reports[35] and our previous work,[30] which may be because GST here is restricted to specific areas rather than in the form of thin films.

Transmission spectra were measured using a Fourier-transform infrared (FTIR) spectrometer (Bruker Vertex 80v) coupled with a confocal microscope (Hyperion 2000), equipped with a 15× objective, a numerical aperture of 0.4 and a liquid nitrogen cooled mercury cadmium telluride detector. A ZnSe polarizer was used to linearly polarize the incident electromagnetic wave. All the spectra were measured with a resolution of 4 cm^{-1} and 256 scans.

Results and discussion

In order to optimize the geometric parameters and to analyze the effect of the GST phase transition process on the transmission spectra, numerical simulations were performed using the commercial simulation software, Lumerical finite-difference time-domain (FDTD) Solution. The simulation domain includes one unit cell of the structures with periodic boundary conditions in both x and y directions and a perfectly matched layer (PML) absorbing boundaries in the z direction. A plane wave was imposed on the unit cell along the $-z$ direction with x-polarization (as shown in Fig. 1), and the transmission spectra were detected behind the unit cell. In the entire set of simulations, the permittivity of gold was described by the Drude model[45] with plasma frequency $\omega_p = 1.37 \times 10^{16}$ rad s^{-1} and collision frequency $\gamma = 3 \times 4.08 \times 10^{13}$ s^{-1}. The dispersion relationships of GST in the amorphous state (a-GST) and the crystalline state (c-GST) were obtained using an ellipsometer, as shown in Fig. 2. In a range of 80–200 THz, a significant difference in the refractive index between a-GST and c-GST was observed. The difference of the extinction coefficient was the least near 100 THz, indicating the lowest loss of c-GST. Therefore, the resonance frequency is controlled near the low loss range.

Simulated transmission spectra are shown in Fig. 3(a) and (c). As shown in the spectra, a transparent window with a transmission amplitude of more than 0.7 appears at near 103 THz when GST is in the amorphous state both in BMM and DMM. The corresponding experimental data are shown in Fig. 3(b) and (d). It is clear that the simulated results agree well with the measured data. The slight reduction in the transmission peak intensity and broadening of the peak width may be attributed to the imperfections of the metal structures. We can also find from the spectra that, in the two configurations, the performances of the frequency shift and the transmission peak intensity reduction of the transparent window are obviously different when GST is transformed into the crystalline state. For BMM, a change in the GST phase causes a small red shift of the transparent window from 103.52 THz to 102.26 THz (1 THz shift) and a slight reduction in the transmission peak amplitude from 0.72 to 0.59. As for DMM, a shift of the transparent window and a reduction in the transmission intensity caused by the change in the GST phase are much more obvious, where the transparent window shifts from 103.34 THz with a transmission amplitude of 0.72 to 97.71 THz with a transmission amplitude of 0.43 (6 THz shift).

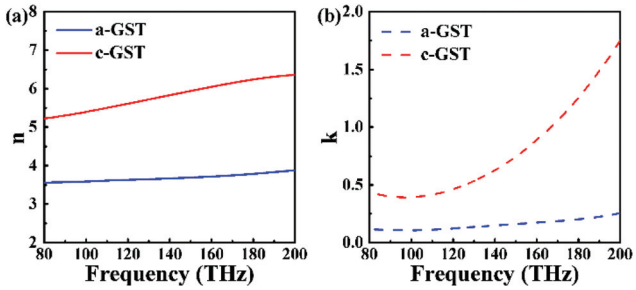

Fig. 2 (a) Refractive index (n) and (b) extinction coefficient (k) of GST in the amorphous (blue line) and crystalline states (red line) measured using an ellipsometer.

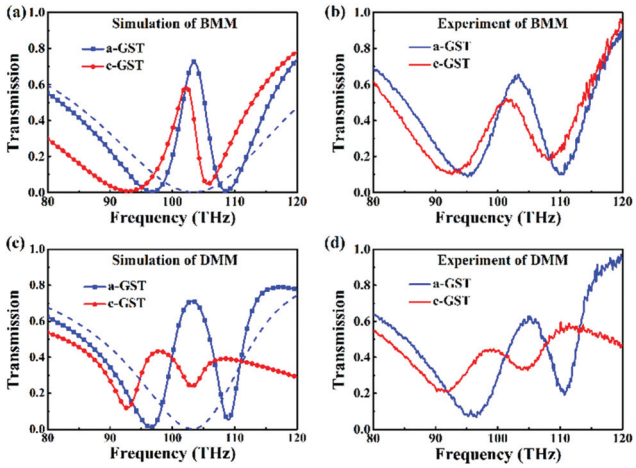

Fig. 3 Simulated and experimental transmission spectra of BMM and DMM. (a and b) Represent BMM and (c and d) represent DMM. The blue and red lines in the spectra show GST in the amorphous state (a-GST) and in the crystalline (c-GST) state, respectively. The blue dashed lines in (a) and (c) represent the transmission spectra of the bright meta-atoms when GST is in the amorphous state.

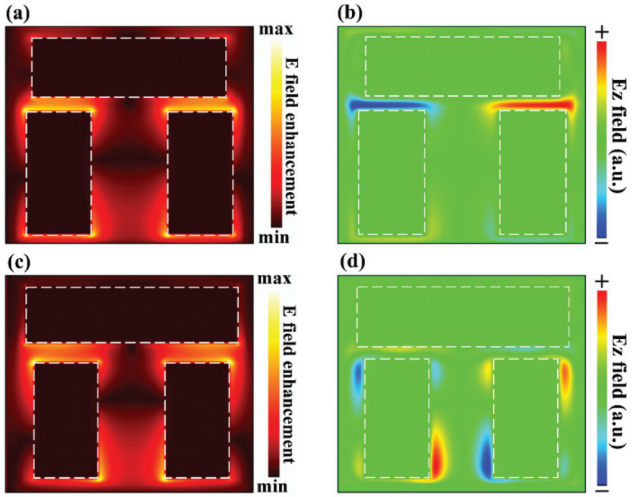

Fig. 4 Electric field intensity and z-component electric field distributions around the transparent window when GST is in the amorphous state, where (a) and (b) represent BMM at 103.52 THz, and (c) and (d) represent DMM at 103.34 THz.

To prove that the transparent window is caused by the EIT-like resonance indeed, the electric field intensity distribution of BMM and DMM at their transparent windows of 103.52 THz and 103.34 THz with a-GST was determined, as shown in Fig. 4, respectively. When only the bright meta-atoms are considered in the BMM and DMM configurations, x-polarized incident light induces an electric dipole resonance in the metal bar, whose transmission spectra are shown in the blue dashed lines in Fig. 3(a) and (c). After introducing the dark meta-atoms, antiparallel charge distribution in the dark meta-atoms can be observed, as shown in Fig. 4(b) and (d), which indicates the excitation of the quadrupole resonance. Meanwhile, the electric field in the bright meta-atoms is almost completely suppressed compared to the case of shielding of the dark meta-atoms.[38,40] Such phenomena demonstrate that destructive interference between the bright and dark resonators causes suppression of the resonance in the bright meta-atoms, resulting in a narrow transparent window in the transmission spectra. It should be noted that the role of GST strips in the structures is to tailor the dielectric environment, so that the resonant frequencies of bright and dark meta-atoms in both BMM and DMM are very close ensuring that the obvious EIT-like resonance can be generated near the resonant frequency of bright meta-atoms.

The simulated results and the measured data reveal that the sensitivities of BMM and DMM to GST phase transition are quite different. To find out the underlying modulation mechanism of GST phase transition on such EIT-like phenomena, the TCMT method was employed to analyse the coupling mode between the bright and the dark meta-atoms quantitatively. Here in this case, we regard BMM (or DMM) as two resonances and two physical port systems. For simplicity, the composite substrate containing a quartz substrate, GST strips and a SiO_2 thin film is considered lossless, and the asymmetry caused by the introduction of GST is weak enough to be neglected. Besides, as mentioned above, resonance in the dark meta-atoms cannot be directly excited by the incident electromagnetic wave, thus the interaction between the incoming wave and the dark resonator is regarded to be zero. In this way, the transmission spectrum of the metasurface excited by a monochromatic wave can be expressed by:[41,43]

$$t = \frac{(j\omega - j\omega_1 + \Gamma_{i1})(j\omega - j\omega_2 + \Gamma_{i2}) + \kappa^2}{(j\omega - j\omega_1 + \Gamma_{i1} + \Gamma_{e1})(j\omega - j\omega_2 + \Gamma_{i2}) + \kappa^2}, \quad (1)$$

where ω_1, Γ_{e1} and Γ_{i1} (or ω_2, Γ_{e2} and Γ_{i2}) represent the resonance angular frequency, radiative decay rate, and nonradiative decay rate of the bright (or dark) meta-atoms, respectively (here Γ_{e2} = 0, which is not shown in the formula), κ denotes the direct coupling coefficient between the bright and dark meta-atoms, and the subscripts 1 and 2 represent the bright and dark modes, respectively. By fitting $|t|$ to the simulated transmission spectra, the characteristic parameters of BMM and DMM can be acquired. In addition, in order to confirm the variation trend of each characteristic parameter during GST phase change, besides GST in the amorphous and crystalline states, the effective permittivities in the intermediate crystallization levels $\varepsilon_{eff}(\lambda)$ were determined using the Lorenz–Lorentz relation[46,47] and used for simulation and fitting. The Lorenz–Lorentz relation is expressed as:

$$\frac{\varepsilon_{eff}(\lambda) - 1}{\varepsilon_{eff}(\lambda) + 2} = m \times \frac{\varepsilon_{c\text{-}GST}(\lambda) - 1}{\varepsilon_{c\text{-}GST}(\lambda) + 2} + (1 - m) \times \frac{\varepsilon_{a\text{-}GST}(\lambda) - 1}{\varepsilon_{a\text{-}GST}(\lambda) + 2}. \quad (2)$$

In this formula, m denotes the crystallization fraction of the GST film ranging from 0% to 100%, and $\varepsilon_{a\text{-}GST}(\lambda)$ and $\varepsilon_{c\text{-}GST}(\lambda)$ represent the permittivities of GST in the amorphous and crystalline states, respectively.

All the simulated and fitting results for different crystallization fractions of GST from 0% (the amorphous state) to 100% (the crystalline state) are shown in Fig. 5. Different intermediate crystallization levels can be realized at different heating temperatures experimentally.[47] The corresponding characteristic parameters of BMM and DMM are listed in Tables 1 and 2, respectively. The resonance frequencies f_1 (f_2) listed in Tables 1 and 2 below satisfy the relation $f_1 = \omega_1/2\pi$ ($f_2 = \omega_2/2\pi$). Therefore, all parameters are in the unit of THz.

The TCMT accurately fits the spectra around the EIT-like transparent windows in the whole process of GST phase transition, as shown in Fig. 5. According to the data provided in Tables 1 and 2, the radiative decay rate Γ_{e1} is much higher than the nonradiative decay rate Γ_{i1} and Γ_{i2} consistently in the two kinds of structures. Therefore, material absorption inside the metal structures and GST strips is much smaller than the radiation from the bright resonance to the far field so that narrow transparent windows can be produced in both BMM and DMM. In addition, κ is much smaller than the resonance frequencies f_1 and f_2, which proves a weak coupling between bright and dark meta-atoms. Except for the commonalities mentioned above, the data in Tables 1 and 2 also show

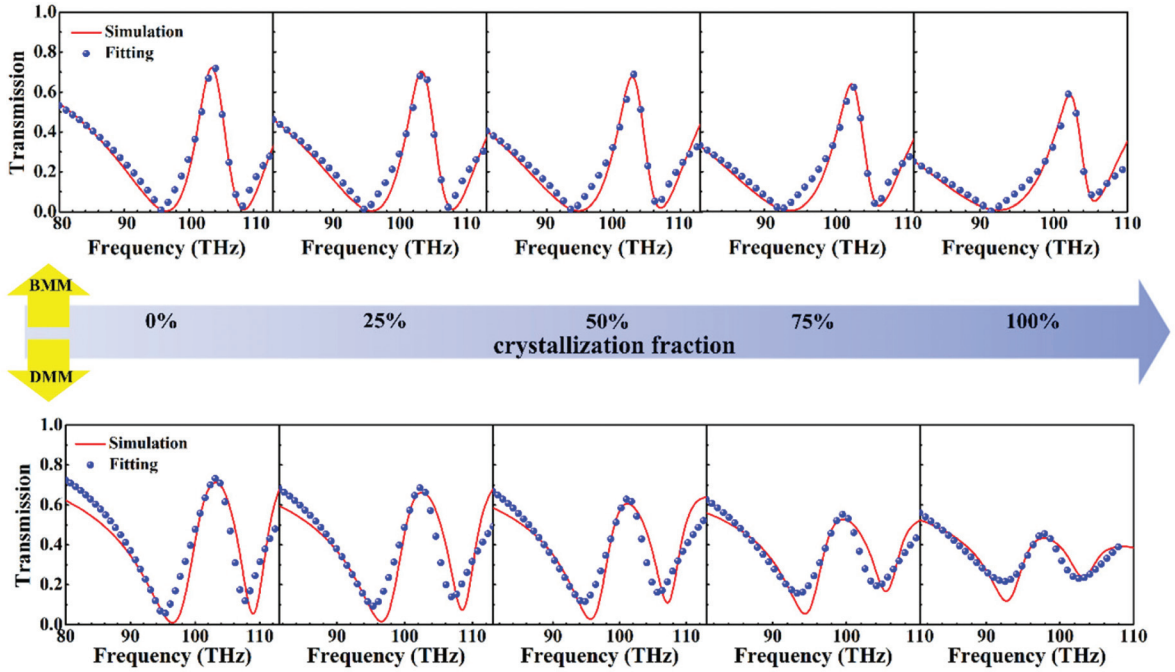

Fig. 5 Simulated and fitting transmission spectra of BMM (the top panel) and DMM (the bottom panel) with the crystallization fraction ranging from 0 to 1. The red lines represent the simulation results and the blue solid circles represent the corresponding fitting data.

Table 1 Characteristic parameters of BMM (unit THz)

Crystallization fraction	f_1	f_2	Γ_{e1}	Γ_{i1}	Γ_{i2}	κ
0	101.08	103.88	28.01	0.56	0.37	5.77
25%	98.66	103.69	29.32	0.79	0.37	5.71
50%	97.26	103.28	30.89	1.18	0.37	5.61
75%	95.37	102.78	33.33	1.59	0.38	5.51
100%	94.00	102.75	38.28	4.47	0.39	5.15

Table 2 Characteristic parameters of DMM (unit THz)

Crystallization fraction	f_1	f_2	Γ_{e1}	Γ_{i1}	Γ_{i2}	κ
0	100.08	103.61	18.10	0.68	0.74	5.94
25%	99.77	102.43	16.87	0.91	1.19	5.62
50%	99.12	101.11	17.00	1.11	1.79	5.38
75%	97.99	99.55	17.28	1.37	2.49	5.01
100%	97.72	97.88	19.07	1.53	3.88	4.70

different variation trends of the characteristic parameters in the two configurations.

For BMM, GST phase transition mainly causes a shift in the resonance frequency of the bright mode from 101.08 THz to 94.00 THz, and meanwhile the decay rate, especially the nonradiative decay rate Γ_{i1}, increases from 0.56 THz to 4.47 THz (about 7 times larger). In contrast, the resonance frequency of the dark mode shifts only about 1 THz, while Γ_{i2} remains basically unchanged. As for DMM, GST phase transition mainly results in the changes in the response of dark meta-atoms, causing the resonance frequency to shift from 103.61 THz to 97.88 THz, and Γ_{i2} to increase from 0.74 THz to 3.88 THz. The changes in the resonance frequency (from 100.08 THz to 97.72 THz, 2 THz shift) and the nonradiative decay rate (from 0.68 THz to 1.53 THz for Γ_{i1}) of the bright meta-atoms are much smaller. In addition, we also found that there is no obvious change in κ during GST phase transition in both BMM and DMM, which means that phase transition has no significant effect on the direct interaction between the bright and dark meta-atoms.

With the continuous GST phase transition, both the refractive index (n) and extinction coefficient (k) increase gradually. An increase in n results in a change in the dielectric environment, causing the red shift of the resonance for the meta-atoms aligned with GST strips. As the GST strips are very close to another kind of meta-atom (tens of nanometers), its phase transition inevitably causes a red shift of the transmission peak, but this red shift is rather small and can become further smaller through increasing the distance from the GST strips. In addition, an increase in k enhances the absorption from the composite substrate, resulting in an increase in the nonradiative decay rate of the corresponding meta-atoms. As shown in Tables 1 and 2, Γ_{i1} is larger than Γ_{i2} for BMM, but it is smaller than Γ_{i2} for DMM, which proves that an increase in the nonradiative decay rate is mainly caused by the GST strips. From the different spectral performances of BMM and DMM before and after GST phase transition, it can be concluded that the resonance frequency and transmission peak intensity of the EIT-like transparent window are mainly determined by the resonance and dissipation of the dark meta-atoms in the EIT meta-

surface. The modulation effect of GST on the dark meta-atoms in DMM is much larger than that in BMM, and therefore more obvious changes can be seen in the EIT-like spectra of DMM.

From another perspective, in addition to the direct heating method, GST phase transition can also be induced by electrical stimuli, in which a controlled and reversible phase transition process can be achieved for the designated GST region. Combining the electrical phase change method with the EIT metasurfaces can further demonstrate its advantage in improving the degree of freedom of active modulation. For example, in an EIT metasurface structure, the GST strip structures can be combined with the bright and dark meta-atoms, respectively, while the layer of a transparent high conductivity material, such as ITO, is deposited on the top of the GST structures as strip electrodes. In this way, the Joule heat generated by ITO electrodes with electrical stimuli can induce a phase change in the amorphous GST,[19] and as a result two different modulation effects can be achieved on a single device by independently controlling the GST strips under the bright and dark meta-atoms, respectively.

Conclusions

In conclusion, we proposed and verified experimentally a new method to separately and independently tune the bright and dark meta-atoms in an EIT system. By introducing GST into strips and combining with a two-step lithography technology, we achieved control over the overall response of the metasurface by adjusting the local part of the structures experimentally. This new active modulation approach greatly increases the flexibility and controllability of tunable metasurfaces. GST strips are separated from each other in space, so that it is possible to control the phase transition degree of each strip independently, which provides a new degree of freedom for active modulation. In addition, taking advantage of the TCMT method, we proved that GST strips mainly have an effect on the meta-atoms aligning with them. With an increase in the refractive index and extinction coefficient of GST during the phase transition process, such an effect is mainly observed as the red shift of the resonant frequency and an increase in the decay rate of the corresponding oscillators. In the EIT metasurface system, the frequency and transmission of the transparent window are mainly affected by the dark meta-atoms, and therefore different performances in the transmission spectra can be observed during GST phase transition for BMM and DMM. This new modulation method is of great help to understand the mechanism of EIT-like resonance active modulation. Besides, different modulation performances of the proposed active metasurfaces will inevitably lead to different transmission phase changes of the structures, which can provide a new route for tunable slow light devices.

Conflicts of interest

There are no conflicts to declare.

Acknowledgements

This work was supported by the National Key Research and Development Program of China (Grant No. 2016YFA0200400, and 2016YFA0200800); National Natural Science Foundation of China (Grant No. 61888102, 11674387, 11504414, 11574369 and 11574385); Strategic Priority Research Program of the Chinese Academy of Sciences (Grant No. XDB33000000) and Key Research Program of Frontier Sciences, CAS (Grant No. QYZDJ-SSW-SLH042).

Notes and references

1 A. E. Minovich, A. E. Miroshnichenko, A. Y. Bykov, T. V. Murzina, D. N. Neshev and Y. S. Kivshar, *Laser Photonics Rev.*, 2015, **9**, 195–213.
2 H. T. Chen, A. J. Taylor and N. Yu, *Rep. Prog. Phys.*, 2016, **79**, 076401.
3 A. V. Kildishev, A. Boltasseva and V. M. Shalaes, *Science*, 2013, **339**, 1232009.
4 C. M. Soukoulis and M. Wegener, *Nat. Photonics*, 2011, **5**, 523.
5 K. Fan and W. J. Padilla, *Mater. Today*, 2015, **18**, 39–50.
6 Q. He, S. Sun and L. Zhou, *Research*, 2019, **2019**, 1849272.
7 L. Kang, R. P. Jenkins and D. H. Werner, *Adv. Opt. Mater.*, 2019, **7**, 1801813.
8 Y. Yao, R. Shankar, M. A. Kats, Y. Song, J. Kong, M. Joncar and F. Capasso, *Nano Lett.*, 2014, **14**, 6526–6532.
9 Y. C. Chang, C. H. Liu, C. H. Liu, S. Zhang, S. R. Marder, E. E. Narimanov, Z. Zhong and T. B. Norris, *Nat. Commun.*, 2016, **7**, 10568.
10 J. Park, J. H. Kang, S. J. Kim, X. Liu and M. L. Brongersma, *Nano Lett.*, 2017, **17**, 407–413.
11 H. T. Chen and W. J. Padilla, *Nature*, 2006, **444**, 597.
12 J. Gu, R. Singh, X. Liu, X. Zhang, Y. Ma, S. Zhang, S. A. Maier, Z. Tian, A. K. Azad, H. T. Chen, A. J. Taylor, J. Han and W. Zhang, *Nat. Commun.*, 2012, **3**, 1151.
13 R. Yahiaoui, M. Manjappa, Y. K. Srivastava and R. Singh, *Appl. Phys. Lett.*, 2017, **111**, 021101.
14 T. Driscoll, H. T. Kim, B. G. Chae, B. J. Kim, Y. W. Lee, N. M. Jokerst, S. Palit, D. R. Smith, M. D. Ventra and D. N. Basov, *Science*, 2009, **325**, 1518–1521.
15 L. Liu, L. Kang, T. S. Mayer and D. H. Werner, *Nat. Commun.*, 2016, **7**, 13236.
16 T. G. Folland, A. Fali, S. T. White, J. R. Matson, S. Liu, N. A. Aghamiri, J. H. Edgar, R. F. Haglund, J. Y. Abate and J. D. Caldwell, *Nat. Commun.*, 2018, **9**, 4371.
17 W. Zhu, R. Yang, Y. Fan, Q. Fu, H. Wu, P. Zhang, N. H. Shen and F. Zhang, *Nanoscale*, 2018, **10**, 12054–12061.
18 B. Gholipour, J. Zhang, K. F. Macdonald, D. W. Hewak and N. I. Zheludev, *Adv. Mater.*, 2013, **25**, 3050.
19 P. Hosseini, C. D. Wright and H. Bhaskaran, *Nature*, 2014, **511**, 206.

20 Q. Wang, E. T. F. Rogers, B. Gholipour, C. M. Wang, G. Yuan, J. Teng and N. I. Zheludev, *Nat. Photonics*, 2016, **10**, 60.
21 K. K. Du, Q. Li, Y. B. Lyu, J. C. Ding, Y. Lu, Z. Y. Cheng and M. Qiu, *Light: Sci. Appl.*, 2017, **6**, e16194.
22 M. Zhu, M. Xia, Z. Song, Y. Cheng, L. Wu, F. Rao, S. Song, M. Wang, Y. Lu and S. Feng, *Nanoscale*, 2015, **7**, 9935–0044.
23 N. Raeis-Hosseini and J. Rho, *Materials*, 2017, **10**, 1046.
24 X. Li, N. Chen, X. Wang and H. Sun, *Adv. Funct. Mater.*, 2018, **28**, 1803380.
25 W. Zhang, R. Mazzarello, M. Wuttig and E. Ma, *Nat. Rev. Mater.*, 2019, **4**, 150.
26 M. Wuttig and N. Yamada, *Nat. Mater.*, 2007, **6**, 824.
27 K. Shportko, S. Kremers, M. Woda, D. Lencer, J. Robertson and M. Wuttig, *Nat. Mater.*, 2008, **7**, 653.
28 F. Ding, Y. Yang and S. I. Bozhevolnyi, *Adv. Opt. Mater.*, 2019, **7**, 1801709.
29 T. Cao, K. Liu, L. Lu, H. C. Chui and R. E. Simpson, *Nanoscale*, 2019, **43**, 20546–20553.
30 C. Li, W. Zhu, Z. Liu, S. Yan, R. Pan, S. Du, J. Li and C. Gu, *Appl. Phys. Lett.*, 2018, **113**, 231103.
31 C. Ríos, P. Hosseini, R. A. Taylor and H. Bhaskaran, *Adv. Mater.*, 2016, **28**, 4720.
32 X. Yin, T. Steinle, L. Huang, T. Taubner, M. Wuttig, T. Zentgraf and H. Giessen, *Light: Sci. Appl.*, 2017, **6**, e17016.
33 P. Pitchappa, A. Kumar, S. Prakash, H. Jani, T. Venkatesan and R. Singh, *Adv. Mater.*, 2019, **31**, 1808157.
34 C. H. Chu, M. L. Tseng, J. Chen, P. C. Wu, Y. H. Chen, H. C. Wang, T. Y. Chen, W. T. Hsieh, H. J. Wu, G. Sun and D. P. Tsai, *Laser Photonics Rev.*, 2016, **10**, 986–994.
35 E. Petronigevic and C. Sibilia, *Opt. Express*, 2016, **24**, 30411–30420.
36 K. J. Boller, A. Imamoğlu and S. E. Harris, *Phys. Rev. Lett.*, 1991, **66**, 2593.
37 S. E. Harris, *Phys. Today*, 1997, **50**, 36–42.
38 S. Zhang, D. A. Genov, Y. Wang, M. Liu and X. Zhang, *Phys. Rev. Lett.*, 2008, **101**, 047401.
39 L. V. Hau, S. E. Harris, Z. Dutton and C. H. Behroozi, *Nature*, 1999, **397**, 594.
40 N. Liu, L. Langguth, T. Weiss, J. Kästel, M. Fleischhauer, T. Pfau and H. Giessen, *Nat. Mater.*, 2009, **8**, 758.
41 Q. Fu, F. Zhang, Y. Fan, J. Dong, W. Cai, W. Zhu, S. Chen and R. Yang, *Appl. Phys. Lett.*, 2017, **110**, 221905.
42 R. Yang, Q. Fan, Y. Fan, W. Cai, K. Qiu, W. Zhang and F. Zhang, *Photonics Res.*, 2019, **7**, 955–960.
43 W. Suh, Z. Wang and S. Fan, *IEEE J. Quantum Electron.*, 2004, **40**, 1511–1518.
44 L. Verslegers, Z. Yu, Z. Ruan, P. B. Catrysse and S. Fan, *Phys. Rev. Lett.*, 2012, **108**, 083902.
45 S. Linden, C. Enkrich, M. Wegener, J. Zhou, T. Koschny and C. M. Soukoulis, *Science*, 2004, **306**, 1351–1353.
46 D. E. Aspnes, *Am. J. Physiol.*, 1982, **50**, 704–709.
47 Y. Qu, Q. Li, K. Du, L. Cai, J. Lu and M. Qiu, *Laser Photonics Rev.*, 2017, **11**, 1700091.